IEEE Access
Multidisciplinary | Rapid Review | Open Access Journal

Received 29 October 2024, accepted 21 November 2024, date of publication 25 November 2024, date of current version 4 December 2024.

*Digital Object Identifier 10.1109/ACCESS.2024.3506053*

RESEARCH ARTICLE

# Modeling Air Pressure Impact on PDIV for Rectangular Wire Turn-to-Turn Insulation of Inverter-Fed Motors Under Different Voltage Waveform Excitations

**HADI NADERIALLAF, MICHELE DEGANO, (Senior Member, IEEE), AND CHRISTOPHER GERADA, (Senior Member, IEEE)**

Power Electronics, Machine and Control (PEMC) Research Institute, University of Nottingham, NG7 2GT Nottingham, U.K.

Corresponding author: Hadi Naderiallaf (Hadi.Naderiallaf@nottingham.ac.uk)

This work was supported in part by the Clean Aviation Joint Undertaking and its Members through the NExt generation high poWer fuel cells for airBORNe applications (NEWBORN) Project, in part by European Union (NEWBORN Project) under Grant 101101967, in part by the U.K. Participants in NEWBORN through the U.K. Research and Innovation (UKRI) under Grant 8219585, and in part by the UKRI Innovate through the Driving the Electric Revolution Innovation Centres (DER-IC) Project under Grant 106233.

**ABSTRACT** This study investigates the partial discharge inception voltage (PDIV) in turn-to-turn insulation of form-wound windings in inverter-fed motors under nine different air pressures, ranging from 1013 mbar to 10 mbar. The research evaluates three voltage waveform excitations: 50 Hz AC, unipolar positive (UP), and bipolar (BP) steep-fronted square waves. The pulse width modulation (PWM) excitations are characterized by a switching frequency of 2.5 kHz, a rise time of 80 ns, and a pulse width of 100 $\mu$s. The experimental analysis focuses on peak and peak-to-peak PDIV values, comparing the variations between 50 Hz AC and PWM excitations across different air pressures. In addition, a novel predictive PDIV model is developed using Schumann's streamer inception criterion (SCSIC) to account for air pressure variations across the three waveform excitations. As another innovation, the model examines streamer inception parameters (SIPs) in rectangular turn-to-turn insulation, incorporating factors such as critical field line length (CFLL), effective ionization coefficient ($\alpha_{\text{eff}}$), partial discharge inception field ($E_{\text{inc}}$), and firing voltage ($V_{\text{firing}}$) under varying air pressures and voltage waveforms. This study provides critical insights into partial discharge phenomena and their potentially destructive effects on rectangular insulated wires. These findings are vital for insulation designers seeking to develop PD-free designs by considering the impact of air pressure, voltage waveform, and variations in SIPs.

**INDEX TERMS** Aerospace testing, electric machines, finite element analysis, insulation, modeling, partial discharges, reliability.

## I. INTRODUCTION

Partial discharge (PD) is a critical end-of-life criterion for the winding insulation of electrical machines, especially when using Type I insulation (organic insulation material) [1]. Among the various insulation sub-systems, turn-to-turn winding insulation is the most vulnerable due to interactions between the steep-fronted voltage waveforms of the inverter and the winding. This results in an uneven voltage distribution, with the most significant voltage drop occurring at the initial turns. PD can occur if the electric field between the turns exceeds the partial discharge inception field (PDIF) [2]. This risk is heightened in random wound windings where the first and last turns may be in close proximity. Therefore, in automotive applications, Type I insulated windings must be designed to ensure the maximum possible voltage peak

The associate editor coordinating the review of this manuscript and approving it for publication was Xiao-Sheng Si.

across turn-to-turn insulation is below the minimum partial discharge inception voltage (PDIV) [1]. Type II insulations, comprising mixed organic and inorganic materials, offer a viable solution for automotive applications by moderately withstanding PD activity at ground level [3]. For aerospace applications, neither Type I nor commercial Type II insulation can withstand PD activity, leading to breakdown in less than five minutes [4].

**FIGURE 1. Depiction of coil windings fabricated using edgewise-insulated wires on the university of nottingham's production line.**

This is due to the reduced air pressures in aerospace environments, which decrease PDIV and drastically increase PD activity's harmful effects [5]. Consequently, for aerospace applications, inverter-fed motor insulation systems must be designed to be PD-free, limiting the maximum feasible DC bus voltage of the inverters well below the targeted levels [4].

One solution to mitigate PD in aerospace applications is using form-wound winding with rectangular insulated wires, such as edgewise or hairpin configurations. This approach offers more manageable inter-turn voltage stress and higher PDIV for turn-to-turn insulation due to the thicker insulation of the wires. The thicker insulation does not reduce power density, as the rectangular wires achieve a higher slot fill factor. Fig. 1 depicts typical coil windings produced using edgewise-insulated wiring. However, even in form wound windings, turn-to-turn insulation remains the most vulnerable compared to phase-to-phase and phase-to-ground insulation [6]. Inter-turn voltage stress in form-wound windings can exceed 1 kV [7], promoting PD inception at the reduced air pressures typical in aerospace applications [5]. Therefore, addressing PD threats in turn-to-turn insulation is critical in designing coil windings for inverter-fed motors in aerospace applications.

Currently, no standards exist for winding insulation design in aerospace applications. Commonly used standards, such as [1], pertain only to industrial drives at ground level and contain discrepancies that need resolution before creating an aerospace-specific standard. For instance, this standard reports the peak value of PDIV, whereas the peak-to-peak value should be used in practice, leading to inconsistencies in PDIV measurement references. Additionally, electrical machine designers question the reliability of PDIV values measured under AC excitations when motors are typically fed by pulse width modulation (PWM) excitations from inverters. The literature lacks consensus on PDIV behavior at reduced air pressures. Studies such as [8] and [9] report lower PDIV values under AC excitations than PWM, suggesting using the peak PDIV value under AC excitations as a conservative criterion for inverter-fed motors. Conversely, [10] found lower peak-to-peak PDIV values under PWM excitations, indicating that using AC excitation values may be risky for aerospace applications. A fast, accurate predictive model for PDIV would greatly aid insulation designers in adhering to PD-free criteria, saving time and money and reducing the need for extensive PDIV measurements. One effective tool for modeling PDIV and analysing PD activity is the streamer inception criterion. Recent research [5] modelled PDIV and analysed PD behavior for round insulated wires and dry air with 13% relative humidity, examining air pressure down to 100 mbar under AC excitations.

This study addresses the research gap in PDIV modeling and PD analysis for rectangular insulated wires under PWM excitations with varying air pressures. The main contributions are:

(1) Experimentally investigating PDIV for rectangular turn-to-turn winding insulation of inverter-fed motors across air pressures from 1013 mbar to 10 mbar, comparing AC and PWM excitations, both bipolar (BP) and unipolar (UP) steep-fronted square waveforms, and considering both peak and peak-to-peak PDIV values.

(2) Developing a PDIV prediction model based on the Schumann streamer inception criterion (SCSIC) for rectangular turn-to-turn winding insulation of inverter-fed motors as a function of air pressure and under both AC and PWM excitations (BP and UP).

(3) Investigating and analysing PD phenomenology and the associated harmfulness under AC and PWM excitations (BP and UP) as a function of air pressure, using SCSIC-derived streamer inception parameters (SIPs). These parameters include the Schumann constant ($K$), which is the natural logarithm of the critical electron number defining the transition from Townsend to streamer discharge, the critical field line length (CFLL), the effective ionization coefficient of air ($\alpha_{\text{eff}}$), the PD inception field ($E_{\text{inc}}$), and the firing voltage ($V_{\text{firing}}$).

## II. METHODOLOGY

### A. TEST SAMPLE

PDIV tests are conducted on pairs of edgewise insulated wires wrapped in polytetrafluoroethylene (PTFE), representing the turn-to-turn insulation system in form-wound windings of electrical machines, as shown in Fig. 2 [11], [12], [13].

The polyamide-imide insulation of the wires has a relative permittivity ($\varepsilon_{\text{r}}$) of 3.3 and a thermal index (TI) of 200°C. Fig. 3 depicts the dimensions of the bare copper wire, insulation thicknesses on the flatwise, edgewise, and fillet sides, and the fillet radius. Detailed information on measuring these dimensions and $\varepsilon_{\text{r}}$ can be found in [12]. A dataset from five

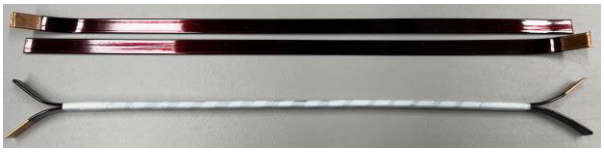

**FIGURE 2.** Illustration of edgewise insulated wires, displaying their condition prior to (top) and following (bottom) PTFE wrapping, representing the test sample.

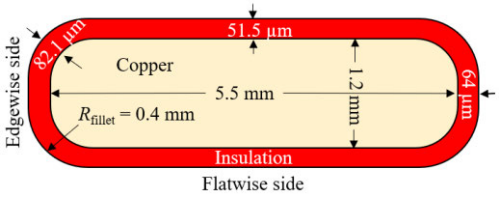


**FIGURE 3.** Diagram showing the cross-sectional dimensions of the edgewise insulated wire being studied.

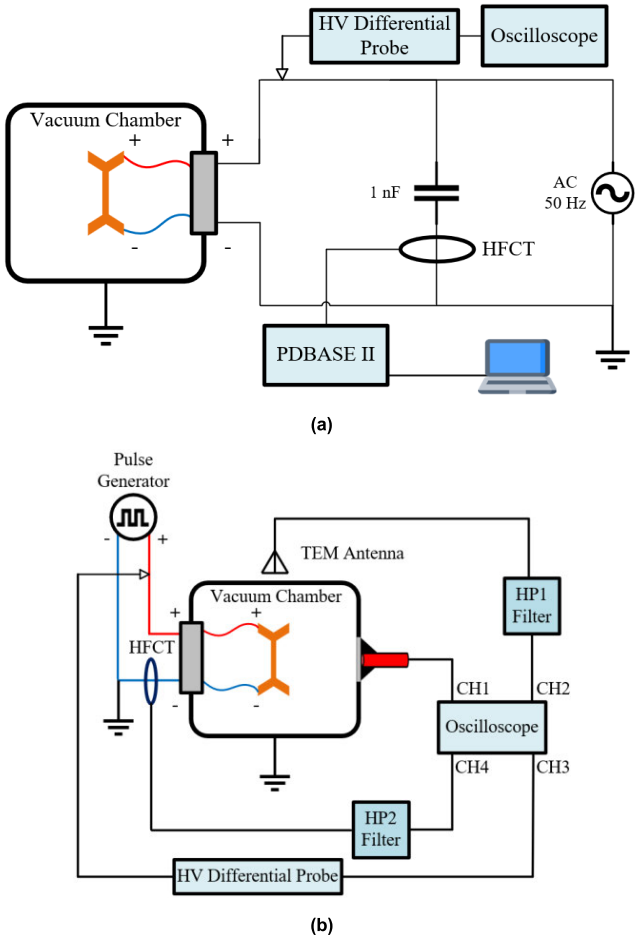


**FIGURE 4.** Diagram illustrating the connection layouts of the PDIV testing setups for (a) AC and (b) PWM excitations.

unused, non-electrically stressed samples is collected for each test condition involving various air pressures and applied voltage waveforms (AC, BP, and UP).

### B. PDIV TEST SETUPS: AC AND PWM

Figs. 4a and 4b display schematic diagrams of the PDIV test setups for AC and PWM excitations, respectively. In both configurations, the voltage applied to the test specimen is measured through a high voltage (HV) feed-through of the vacuum test chamber using a Tektronix THDP0200 HV differential probe, which features a 200 MHz bandwidth. The excitation waveform is monitored via a Tektronix MSO64B oscilloscope with a 4 GHz bandwidth and a 25 GS/s sampling rate.

For PDIV measurement under AC excitations, the AC power supply used is the GW Instek GPT-9802 AC 50 Hz. The PD sensor is a Techimp high-frequency current transformer (HFCT) with a ferrite core and a 1-60 MHz bandwidth. A 1 nF PD-free coupling capacitor is connected in parallel with the test specimen to improve sensitivity and signal-to-noise ratio. The PD signals generated across the test specimen are detected through a conventional indirect circuit where the fast current sensor (i.e., HFCT) is connected in series with the coupling capacitor, as shown in Fig. 4a. The PD signals are acquired and analyzed by the Techimp PD BaseII detector, which has a 16 kHz to 48 MHz acquisition frequency range and a 200 MSa/s sampling rate.

For PDIV measurement under PWM excitations, the RUP6-18bip commercial variable pulse generator system generates UP and BP square voltage waveforms. Three distinct PD sensors monitor PDIV under PWM excitations: 1) a Hamamatsu H10493-012 photomultiplier tube (PMT), 2) a Techimp TEM antenna, and 3) a Pearson 6585 HFCT. Their operating bandwidths are 0-200 kHz, 100 MHz-3 GHz, and 400 Hz-250 MHz, respectively. The PMT is directly connected to the oscilloscope due to its immunity to electromagnetic noise from the fast pulse generator switching. High-pass (HP) filters (150 MHz for the TEM antenna and 50 MHz for the HFCT) help distinguish PD signals from switching noise, as depicted in Fig. 4b.

The measurement of PDIV under PWM using a HFCT is feasible, as shown in [10] and [14]. Both studies employ a wide-band HFCT specifically designed to mitigate switching disturbances from high-frequency power supplies. This is achieved by performing a fast Fourier transform (FFT) on the PWM excitation waveform to identify its maximum frequency content, allowing for the precise selection of a high-pass filter that isolates PD signals while excluding switching noise. Here, a high-bandwidth HFCT (Pearson 6585) with a range of 400 Hz to 250 MHz is used, following the approach in [14]. Coupled with a high-pass filter (CHPFL-0050-BNC), this HFCT effectively separates PD signals from commutation noise, as the filter's 50 MHz cutoff frequency allows disturbances to be filtered while retaining the higher-frequency PD components. The HFCT's wide bandwidth, compared to that used in AC PD setups, further enhances noise exclusion from pulse generator sources in PWM contexts.

To improve measurement sensitivity and reliability, this setup also integrates a TEM antenna and PMT. The TEM antenna, optimized for high-pressure conditions, detects PD signals while the high-pass filter excludes switching disturbances, whereas the PMT is particularly suited for reduced air pressures. Using all three sensors—HFCT, TEM antenna, and PMT—provides reliable, pressure-independent data, validating the sensitivity of the methodology outlined in [14]. For detailed information on HFCT use under PWM, see [10] and [14], and for PMT applications at lower air pressures, refer to [15].

The peak and peak-to-peak values of PDIV are confirmed and recorded once PD is detected promptly by any sensor. A detailed explanation of the variation in sensitivity for different sensors, including HFCT, alternative optical, and UHF detection systems, for PDIV measurements as a function of air pressure is provided in [8].

### C. PDIV TESTING CONDITIONS AND PROCEDURES

The PDIV measurements are conducted at nine air pressure levels: 1013, 800, 600, 200, 150, 100, 50, 25, and 10 mbar, all at a constant temperature of 25°C. Humidity is monitored and set at an absolute humidity (AH) of 13.84 g/m$^3$, corresponding to relative humidity (RH) of 60% at 25°C and 1013 mbar [4]. As air pressure decreases, RH also decreases because gas solubility, including moisture content in the air, reduces with lower pressure, according to Henry's law [16]. Accordingly, RH values are carefully monitored and recorded at nine selected air pressures. The recorded values, ranging from 1013 mbar to 10 mbar, are 60%, 53.4%, 45.5%, 29.7%, 27.7%, 25.7%, 23.7%, 22.7%, and 14%.

The air pressure range from 1013 mbar to 10 mbar is selected primarily to enable comparison with prior studies, such as [8], which model PDIV as a function of air pressure. The choice of 150 and 200 mbar specifically aims to validate the SCSIC method for estimating PDIV at air pressures corresponding to cruising altitudes in aerospace applications, across various voltage waveform excitations, including AC and PWM. Furthermore, investigating lower pressures, down to 10 mbar with high-resolution intervals, seeks to determine the lowest pressure at which the SCSIC method remains effective.

For each air pressure level in the test campaigns, PDIV is measured under three different voltage excitations: AC 50 Hz, UP, and BP square waveforms. The switching frequency, rise time, and pulse width duration of the PWM waveforms (UP and BP) are 2.5 kHz, 80 ns, and 100 $\mu$s, respectively.

To measure PDIV, the voltage peak is incrementally raised by 10 V, with varying waiting times between steps as quantified in Table 1 [5]. The extended waiting times at lower air pressures are necessary because PD initiation relies on two conditions coinciding: exceeding the electric field in the air wedge from the PD inception field and the availability of a free electron to initiate the PD event through reaching the critical avalanche size. Lower air pressures reduce the possibility of this occurrence due to the reduced gas number density [5], [17]. It is important to note that following the approach proposed in [8], some results may not be directly comparable to previous studies that employed a constant voltage rise rate to detect PDIV across varying air pressures. Using a constant rise rate, without accounting for the changes in discharge mechanisms at lower air pressures and the reduced probability of reaching the critical avalanche size along the CFL, introduces a positive error, resulting in an overestimation of PDIV at reduced pressures.

Additionally, since one of the objectives of this study is to analyze SIPs along the actual CFL, the waiting time between voltage steps has been increased to account for the reduced probability of reaching the critical avalanche size as air pressure decreases. The waiting times listed in Table 1 correspond to those reported in [8], with an extrapolated value for 10 mbar, which was not covered in [8].

**TABLE 1. Waiting times between voltage steps in PDIV tests as a function of air pressure.**

| Air pressure (mbar) | 1013 | 800 | 600 | 200 | 150 | 100 | 50 | 25 | 10 |
|---|---|---|---|---|---|---|---|---|---|
| Waiting time (minutes) | 0.5 | 0.7 | 1 | 4 | 4.6 | 6 | 10 | 20 | 30 |

PDIV tests are conducted once for each unused sample. While at ground level, repeated PDIV measurements on the same sample after short exposure (e.g., one minute) can yield comparable results, as PD activity over a brief period may not significantly affect the insulation or subsequent PDIV values, this approach is not suitable at reduced air pressures. At low pressures, the lifespan of insulated wires, including corona-resistant insulation (Type II), under PD activity is on the order of seconds, as reported in [4]. In this study, the wire is insulated with polyamide-imide (Type I), an organic insulation that is more susceptible to damage from PD activity, particularly at low air pressures [18]. Repeated PDIV measurements under these conditions result in progressively lower PDIV values due to insulation degradation. To maintain consistency, each specimen is tested only once, from 1013 mbar down to 10 mbar. This approach also prevents any reduction in PDIV values caused by residual charges from previous tests, as noted in [19], and [20].

For each case study (i.e., a combination of air pressure and specific voltage waveform excitation), five pristine specimens are tested to gather data. Using five PDIV values per case study provides the minimum data points required for statistical analysis. With nine air pressure levels and three waveform excitations, a total of 135 samples are tested to complete the dataset. This selection of five samples per case study balances the need for sufficient data with the practical time constraints of PDIV testing, especially at lower air pressures, where longer waiting times between voltage steps are necessary. Consequently, the dataset derived from testing

five unused pairs of PTFE-wrapped edgewise insulated wires is subjected to post-analysis using a 2-parameter Weibull distribution. The reported peak and peak-to-peak PDIV values corresponding to each combination of voltage waveform and air pressure are the $10^{th}$ percentile (B10) values extracted from this distribution, fitted to the measured PDIV peak and peak-to-peak values. B10 is selected as a reference since the reliability of the insulation system is typically evaluated by selecting specific percentiles from the distribution tail [21], [22]. The B10 of the PDIV peak, calculated from the non-exceedance probability in Weibull distributions, acts as a benchmark for determining the SIPs.

## III. MODELING PDIV AND SIPs USING SCSIC

As a preliminary hypothesis, it is assumed that streamer discharges are mainly responsible for dielectric degradation from ground level to cruising altitude [5]. One might argue that as air pressure decreases, discharges shift from streamer to Townsend discharges, necessitating two different inception criteria: one for higher air pressure and one for lower air pressure. However, it should be noted that the energy of Townsend discharges is lower than that of streamer discharges. As experimentally demonstrated in [4], even corona-resistant insulating materials, which can withstand PD moderately at atmospheric pressure, cannot withstand PD at reduced air pressures. This is because the decrease in air pressure significantly increases the destructive potential of PD. Therefore, even at reduced air pressures, insulation degradation as a consequence of PD cannot be solely attributed to Townsend discharges, which have lower energy content compared to streamer discharges. Thus, the streamer criterion is accepted as a reliable tool for predicting PDIV at different temperatures and air pressures [8].

Initially, electrical discharges are of the Townsend type. When the electron count at the head of an avalanche reaches a critical threshold, fast-moving filamentary streamers form, marking the transition from Townsend to streamer discharges in the air [23]. According to the SCSIC, this transition occurs when condition (1) is satisfied along at least one electric field line in the air gap [24].

$$K \leq \int_0^{x_c} \alpha_{\text{eff}}(x) \cdot dx \tag{1}$$

In (1), $K$ is a dimensionless quantity representing the natural logarithm of the critical electron number that defines the transition from Townsend to streamer discharge. The variable $x$ denotes the distance an initial electron travels along the field line from the cathode to the anode within the air gap. The critical distance $x_c$ is the point beyond which filamentary streamers rapidly propagate from the avalanche's head, signifying the transition from Townsend to streamer discharge. $\alpha_{\text{eff}}$ is the effective ionization coefficient of air along the electric field lines, as given by (2). The effective ionization coefficient of air, denoted as $\alpha_{\text{eff}}$, is determined across each field line and is calculated by (2):

$$\alpha_{\text{eff}} = \alpha - \eta \tag{2}$$

In (2), the ionization coefficient ($\alpha$) and attachment coefficient ($\eta$) of air depend on factors such as electric field intensity, altitude or air pressure, temperature, and humidity [5], [17], [21]. Both $\alpha$ and $\eta$ are dependent on the electric field intensity. As an electron moves from the cathode to the anode along the electric field lines, variations in field intensity lead to changes in these coefficients. $\alpha$ and $\eta$ can be computed as functions of the reduced electric field using BOLSIG+ software [25], [26].

### A. DERIVING SIPs UNDER PDIV

For any insulation subsystem of the electrical machine, such as turn-to-turn insulation, the electric field distribution in the air wedge between two adjacent rectangular insulated wires is computed using FEM simulation with PDIV as the applied voltage. Then, the effective ionization coefficient of air for the given environmental conditions (air pressure, temperature, and humidity) is calculated by considering the electric field intensity along each field line. Next, the integral on the right-hand side of (1) is calculated for all the electric field lines to find its maximum value under PDIV. This maximum value is identified as the Schumann constant ($K$), which serves as the first SIP and is used to predict PDIV based on SCSIC. The length of the electric field line that yields the maximum value of the right-hand side of (1) is defined as the second SIP, known as the critical field line length (CFLL). Other SIPs are related to the CFLL, such as the effective ionization coefficient ($\alpha_{\text{eff}}$), the electric field intensity known as the PD inception field ($E_{\text{inc}}$), and the voltage across the CFLL known as the firing voltage.

In this study, SIPs are derived under three different voltage waveform excitations: AC, bipolar (BP), and unipolar (UP) steep-fronted square waveforms. The electric field distribution is governed by the permittivity of the wire insulation in the air wedge between two adjacent insulated wires under both AC and PWM excitations. The peak voltage, regardless of waveform, solely determines the maximum instantaneous electric field intensity along each field line in the air wedge. Under PWM excitations, the instantaneous peak of the voltage drop in turn-to-turn insulation (i.e., voltage overshoot) depends on the rise time of the steep-fronted waveform and the cable length. This peak voltage stress should be considered lower than PDIV to adhere to the PD-free design of electrical machines [1]. To calculate the maximum instantaneous electric field distribution along each electric field line resulting from the instantaneous voltage peak, FEM electrostatic simulation is performed using COMSOL software, as shown in Fig. 5 for a 1 V peak.

It should be noted that these simulations are simplified and do not account for potential space charge accumulation under UP square wave excitation, as detailed in [27].

The essential steps for calculating SIPs are outlined below [5], [11], [12], [17], [21]:

a) Configure the voltage in electrostatic simulations to match the peak of the measured PDIV for the specific voltage

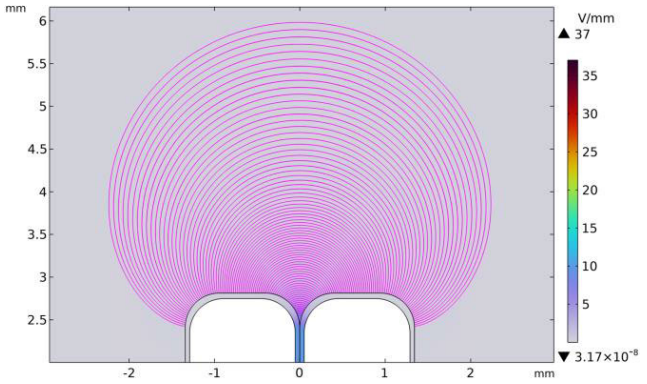


**FIGURE 5.** 2D COMSOL multiphysics® simulation of the electric field distribution between rectangular turn-to-turn insulation.

waveform under study (AC, BP, or UP), also taking into account the desired probability, for example, 10% (B10).

b) Under the B10 probability of the PDIV peak, perform a 2D electric field distribution simulation between the two insulated wires in the air wedge to calculate the electric field intensity, E(x,y), along the field lines. Another output of the simulation is the field line length (FLL) of the electric field lines extending only in the air. The inputs for the FEM software (COMSOL) include the wire dimensions (cross-section and insulation thickness) and the insulation's relative permittivity ($\varepsilon_r$).

c) Convert the electric field intensity obtained in step (b) to the reduced electric field ($E/n$). The gas number density ($n$), which varies with air pressure and temperature, necessitates the consideration of the reduced electric field rather than the absolute electric field intensity. The ideal gas law, (3), expresses gas number density (n) in $m^{-3}$.

$$n = p \cdot V / k_B \cdot T \tag{3}$$

In (3), $p$ denotes pressure in Pascals, $V$ signifies the volume under test in cubic meters (e.g., the volume of the vacuum chamber), $T$ stands for temperature in Kelvin, and $k_B$ represents the Boltzmann constant ($1.380649 \times 10^{-23}\ J/K$).

d) Use BOLSIG+ software [25], [26] to derive $\alpha$ and $\eta$ as functions of the reduced electric field along each field line, considering the temperature and humidity of the air obtained in step (c). Then, use (3) to calculate $\alpha_{eff}$ across each field line in the air wedge.

e) Using the FLLs obtained in step (b) and $\alpha_{eff}$ from step (d), compute the right-hand term in (1) for all field lines in the air wedge.

f) Report the maximum value obtained in step (e) as the first SIP, denoted as $K$, corresponding to the specified air pressure and voltage waveform under investigation.

g) Additionally, report the FLL at which the maximum right-hand term in (1) is achieved as CFLL, the electric field at CFLL as the PD inception field ($E_{inc}$), and the voltage across CFLL, calculated by multiplying $E_{inc}$ and CFLL, denoted as the firing voltage ($V_{firing}$).

To gain a clearer understanding of the methodology used for calculating $K$, which acts as the initial SIP serving as a reference for deriving others, refer to Fig. 6. This figure illustrates the process of determining the maximum right-hand term in (1), denoted as $K$. It illustrates the $K$ values obtained under BP excitation at air pressures of 1013 mbar, 200 mbar, 100 mbar.

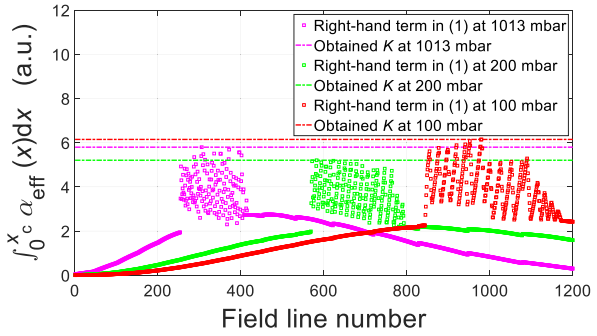


**FIGURE 6.** A typical representation of the $K$ determination process under BP excitations, at 1013, 200 and 100 mbar, and room temperature (25°C).

In Fig. 6, the field line numbering progresses from shortest to longest. Consequently, it is observed that as air pressure decreases from 1013 mbar to 100 mbar, the field line where the maximum value of the right-hand term in (1) occurs extends. This indicates that at reduced air pressures, PD events transpire along longer field lines. Consequently, electrons within the avalanche gain heightened kinetic energy as they traverse a longer discharge path, intensifying PD destructive potential at lower air pressures [5], [17]. Moreover, Fig. 6 highlights a critical zone where $\alpha_{eff}$, and consequently, the right-hand term in (1), experience a notable increase. This critical region significantly influences the determination of $K$, as the maximum value of the right-hand term in (1) is attained within it [5], [11], [12], [17], [21].

### B. PDIV ESTIMATION APPROACH

PDIV estimation is conducted using the derived $K$ values via the SCSIC for three different voltage waveform excitations (AC, BP, and UP) at nine different air pressures (1013, 800, 600, 200, 150, 100, 50, 25, and 10 mbar). The main steps of the iterative algorithm for predicting PDIV are summarized below:

a) Allocate the $K$ value corresponding to the designated voltage waveform and air pressure. This $K$ value corresponds to the targeted probability. For instance, if the chosen $K$ value originates from the $10^{th}$ percentile of the measured PDIV values fitted to the Weibull distribution, this $K$ will yield a PDIV occurrence probability of 10%, as used in this study [11].

b) Under a unit voltage peak, determine the electric field distribution within the air wedge between two rectangular insulated wires, extending from the near fillet side to the far fillet side, as illustrated in Fig. 5. For the electrostatic FEM simulation, consider the cross-sectional geometric

dimensions of the wire (e.g., insulation thickness and copper dimensions) and the insulation relative permittivity ($\varepsilon_r$), which governs the electric field distribution in the air gap. Configure the COMSOL settings to arrange the electric field intensities from strongest to weakest, corresponding to the shortest to longest field lines, and document this field distribution as $E_{\text{database}}(x, y)$ [5], [11], [12], [17], [21].

c) Start the iterative algorithm with an initial voltage significantly below PDIV, such as 50 V.

d) As voltage increases, the electric field intensity along each field line rises linearly. Therefore, for the selected voltage peak value as PDIV, calculate the electric field intensity across each field line ($E(x, y)$), using the principle of linearity as given by (4), and revise the database obtained from step (b).

$$E(x, y) = PDIV \cdot E_{\text{database}}\,(x.y) \tag{4}$$

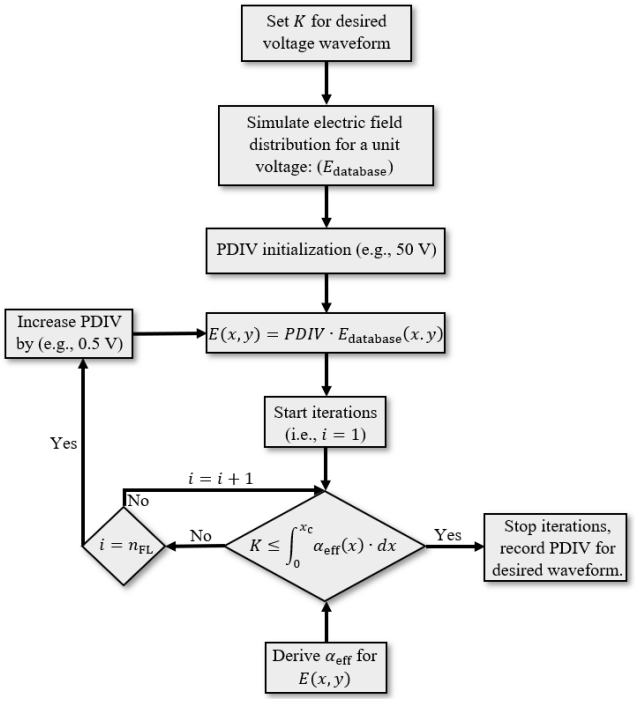


**FIGURE 7. Flowchart illustrating the iterative procedure for constructing the PDIV predictive model under varied AC and PWM voltage waveform excitations across various air pressures.**

e) Deriving $\alpha_{\text{eff}}$ along each field line requires converting the output from step (d) to the reduced electric field. This involves (3) ascertaining the gas number density ($n$) at the investigated air pressure and temperature. Next, the obtained electric field intensity database from step (d) is divided by ($n$) to deduce the reduced electric field along each field line, thus $E(x, y)/n$.

f) Upon determining the reduced electric field along each field line, $\alpha_{\text{eff}}$ can be computed using the BOLSIG+ software. This software provides $\alpha$ and $\eta$ as functions of the reduced electric field at the investigated temperature and humidity [25], [26]. Using (2), $\alpha_{\text{eff}}$ as a function of the reduced electric field can be calculated. As a result, $\alpha_{\text{eff}}$ can be derived across each field line concerning $E(x, y)/n$.

g) Using the chosen PDIV value and the predetermined $K$ value from step (a), evaluate if condition (1) is fulfilled for at least one electric field line in the air wedge. If so, designate the selected voltage as the estimated PDIV, with the probability linked to $K$ corresponding to the assigned voltage waveform type and air pressure.

h) If condition (1) from step (g) is not met, it indicates that the selected PDIV value is insufficient. In this case, increment the voltage by, for example, 0.5 V, and repeat the procedure starting from step (d) until the condition (1) in step (g) is satisfied, ensuring the attainment of PDIV with the desired probability under the specified voltage excitation and air pressure.

It is important to clarify that while using two distinct data sets for deriving $K$ and predicting PDIV appears more reasonable, in practice, one would logically select two comparable data sets for these calculations. In other words, for a specific environmental condition, using pristine and identical test samples ensures that the statistical distribution from different data sets would be comparable. This means that even if separate data sets are employed, as long as they are comparable, the PDIV error derived from one will be similar to that from the other. Therefore, this study employs a single data set for both $K$ calculation and PDIV prediction, consistent with the approach used in other references such as [28] and [29].

Fig. 7 depicts a flowchart outlining the iterative process of developing the predictive model for PDIV under different AC and PWM excitations across varying air pressures. In the iterative process depicted in Fig. 7, it's crucial to consider the optimal number of electric field lines in the air wedge, denoted as $n_{\text{FL}}$, to ensure a separation distance of no more than 1 $\mu$m between lines. This value varies with factors such as the conductor diameter, insulation thickness, and fillet radius at the corner side of the rectangular wire. The determination process, as outlined in [5] and [30], involves conducting FEM simulations with an extremely fine mesh size to accurately assess the configuration.

## IV. EXPERIMENTAL RESULTS AND DISCUSSIONS

### A. MEASURED PDIV

Figs. 8a and 8b present the 10$^{\text{th}}$ percentile of measured PDIV peak-to-peak and PDIV peak values, respectively. The PDIV peak-to-peak value is used for insulation qualification testing and determines the end-of-life of insulation systems through accelerated thermal aging. Conversely, the PDIV peak value is crucial for the PD-free design of electrical machines, allowing for the computation and comparison of the peak voltage with the PDIV peak. Therefore, both peak-to-peak and peak PDIV values are reported here (Figs. 8a and 8b).

In [31], the behavior of the electric field in the air gap between two insulated wires under UP and BP excitations was explained in detail. When PDIV measurements are referenced to the peak-to-ground value, the PDIV peak under UP

excitations is higher than that under BP and AC excitations. It is important to note that, in practice, steep-fronted waveforms like UP and BP are not overshoot-free. For example, under positive UP excitation, a negative voltage overshoot occurs during the falling edge, as shown in [27]. Consequently, the peak-to-peak PDIV value exceeds twice the peak PDIV value. Additionally, space charge accumulation influences both the peak and peak-to-peak voltages across the air gap, varying with exposure time [27]. For BP excitations, if the inverter produces a perfectly symmetric waveform, the peak-to-peak PDIV should be approximately twice the peak value. However, asymmetry in BP excitations can lead to unequal positive and negative peak voltages. In contrast, AC excitations, being symmetric, result in a peak-to-peak PDIV that is exactly twice the PDIV peak.

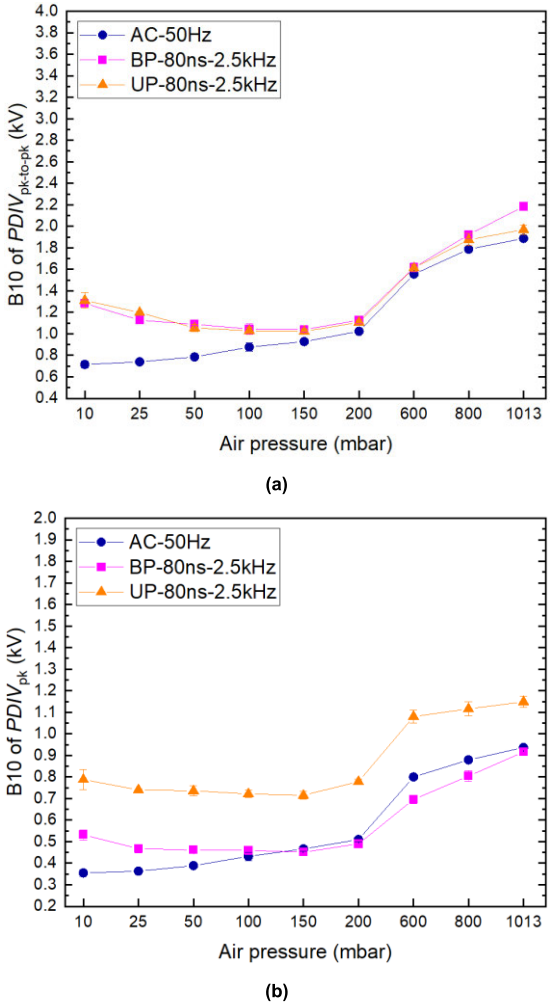


**FIGURE 8. Measured B10 of (a) PDIV peak-to-peak and (b) PDIV peak under three distinct excitations (AC, BP, and UP), as a function of air pressure. Confidence intervals with a 95% probability are also provided.**

Fig. 8a shows that at ground level (1013 mbar), the measured PDIV peak-to-peak varies slightly with the type of voltage waveform excitation, being highest under BP and lowest under AC. The lower PDIV peak-to-peak under UP compared to BP at 1013 mbar aligns with findings in [32] and is attributed to space charge accumulation under UP excitations [27]. The ratios of PDIV peak-to-peak under BP and UP to AC are 1.15 and 1.04, respectively, at 1013 mbar.

From 1013 mbar down to 10 mbar, AC consistently shows the lowest PDIV peak-to-peak, suggesting its use as a conservative reference for insulation qualification compared to PWM excitations. While PDIV peak-to-peak in AC decreases steadily from 1013 mbar to 10 mbar, under PWM excitations, it decreases only to 150 mbar before increasing at lower pressures. The increase in PDIV under PWM excitations at reduced air pressures is due to the combined effects of lower gas density and rapid voltage rise times. For PD inception to occur at low pressures, three conditions must be met: 1) the electric field must exceed the PDIF, 2) a free electron must be present, and 3) a critical electron avalanche must form as the electron travels from cathode to anode. For the third condition, two key factors are necessary: the electric field must stay above PDIF long enough, and sufficient gas molecules must be available along the electron's path to sustain ionization and allow the avalanche to reach a critical size, thus triggering a PD event.

At pressures below 150 mbar, under PWM excitations, the first two conditions cannot occur simultaneously at the same voltage peak, as they do at higher pressures. This necessitates a higher voltage to achieve the critical avalanche size. For instance, at 10 mbar, if the PWM voltage peak is set to the PDIV level observed at 150 mbar, the fast rise time and reduced gas density prevent the electron avalanche from reaching the critical size required for PD. Therefore, the applied voltage at 10 mbar must be increased to keep the electric field above PDIF for long enough and ensure sufficient ionization to reach critical avalanche size. As a result, PDIV increases under PWM excitations at pressures below 150 mbar.

In contrast, with AC excitations, the longer rise time allows the electric field to remain above PDIF for a more extended period compared to PWM excitations at the same peak field. Consequently, PDIV under AC excitation decreases consistently as air pressure drops from ground level to 10 mbar.

Consequently, at the lowest air pressure (10 mbar), the PDIV peak-to-peak in AC is significantly lower than in PWM, with a ratio of 0.55. At 200 mbar, equivalent to a cruising altitude of 38.6k ft, the PDIV under AC is comparable to PWM, with a ratio of 0.9.

Fig. 8a shows that at reduced air pressures below 800 mbar, the measured PDIV peak-to-peak under BP and UP excitations, with the same switching frequency and rise time, are comparable. This indicates that PDIV is less affected by space charge accumulation under UP excitations in this pressure range. This can be attributed to the higher concentration of the electric field in air rather than in solid insulation at lower pressures. Consequently, the role of the solid dielectric and its characteristics, such as space charge accumulation, becomes less significant at reduced air pressures [5], [33].

It is important to note that in real-world applications, higher altitudes result in increased electron availability due to natural radiation, a condition that is challenging to replicate in ground-based laboratories. Furthermore, space charge accumulation at reduced air pressures may differ from that observed at ground level under the same peak applied UP excitations.

As expected, Fig. 8b displays that the measured PDIV peak under UP excitations is higher than under BP excitations with the same rise time and switching frequency and under AC 50 Hz [34]. Similar to PDIV peak-to-peak, the PDIV peak under PWM excitations decreases with air pressure reduction, reaching its lowest value at 150 mbar, and then increasing at lower pressures. Under AC excitations, PDIV consistently decreases with air pressure reduction.

Interestingly, at ground level (1013 mbar) and air pressures of 200 mbar and 150 mbar (cruising altitudes of 38.6k ft and 44.3k ft), the measured PDIV peak under BP and AC excitations are comparable, though slightly lower for BP. Between 200 mbar and 1013 mbar (600 and 800 mbar), the PDIV peak under BP is lower than that under AC 50 Hz, with ratios of 0.91 and 0.87 at 800 and 600 mbar, respectively. It is important to note that these ratios are derived using the B10 values of PDIV as the reference, although the B10 values lie outside the 95% confidence interval. Furthermore, these ratios are based on datasets consisting of five data points for each case study, defined by a specific combination of air pressure and voltage waveform. Fig. 8b also shows that below 100 mbar, the difference between PDIV peaks under AC and BP excitations becomes more pronounced. At these low pressures, while PDIV under AC continues to decrease, PDIV under BP starts to increase, resulting in lower PDIV under AC than BP at 10 mbar, with a ratio of 0.67.

Figs. 8a and 8b demonstrate that PDIV peak-to-peak under AC excitations can be used for conservative testing and insulation qualification in aerospace applications. However, for PD-free design at air pressures such as 800 and 600 mbar, relying on the measured PDIV peak under AC excitations to design inverter-fed motors would be risky. Therefore, for air pressures between ground level and a cruising altitude of 38.6k ft (200 mbar), it is recommended to use the measured PDIV peak under the same PWM excitation as used in practice as the reference for PD-free design of inverter-fed motors in aerospace applications.

At air pressures of 200 mbar and 150 mbar (cruising altitudes of commercial aeroplanes) and 1013 mbar (automotive applications), the PDIV peak under AC is very close to that under BP. Therefore, for aerospace and automotive applications, the measured PDIV peak under AC excitations can be used as a reference to consider the PD-free criterion in designing inverter-fed motors.

### B. SCHUMANN CONSTANT (K)

Fig. 9 presents the obtained maximum $K$ values under PDIV as a function of air pressure for various voltage waveform excitations, including AC 50 Hz, BP, and UP. The results show a direct correlation between the PDIV peak (Fig. 8b) and the $K$ values, where higher PDIV peaks correspond to higher $K$ values. For example, across all air pressures, $K$ values under UP excitations are consistently higher than those under BP and AC excitations due to higher PDIV peaks in UP. This indicates a larger avalanche size under UP excitation compared to AC and BP. However, the difference in the obtained $K$ values under AC and BP excitations from ground level to 50 mbar is so subtle that it may be obscured by experimental errors.

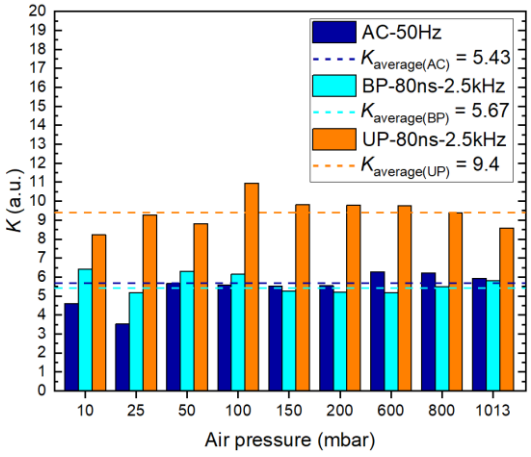


**FIGURE 9.** Derived $K$ under B10 of PDIV peak for three distinct excitations (AC, BP, and UP), with respect to air pressure.

From 1013 mbar to 150 mbar, $K_{AC}$ is slightly higher than $K_{BP}$ because of the marginally higher PDIV peak in AC within this range (Fig. 8b). Below 100 mbar, $K_{BP}$ surpasses $K_{AC}$ as the PDIV peak for BP overtakes that for AC. Additionally, Fig. 9 reports the average $K$ values from 10 mbar to 1013 mbar for AC, BP, and UP excitations, which are 5.43, 5.67, and 9.4, respectively.

The lower average $K$ values under AC excitations compared to PWM excitations from 10 to 1013 mbar suggest that using $K_{AC}$ for PDIV predictions under PWM excitations would result in conservative estimates. The comparison of $K$ values from 1013 mbar to 10 mbar for each voltage waveform reveals that the highest $K$ is achieved at different air pressures depending on the excitation type: 600 mbar for AC, 10 mbar for BP, and 100 mbar for UP.

As demonstrated in [28], the variation in $K$ across different magnet wires at ground level is negligible, leading to the proposal of an average $K$ value of 5.98 for PDIV prediction. This finding suggests that the stability of $K$ can be a useful feature for PDIV prediction. If $K$ were to change significantly with environmental conditions (such as air pressure), the SCSIC would be ineffective for PDIV prediction. However, as shown in Fig. 9, $K$ remains relatively stable, especially during polarity reversals in excitation (e.g., AC and BP), even as PDIV varies with air pressure. This quasi-stability of $K$

supports the reliability of the SCSIC for predicting PDIV across different air pressures.

When comparing the SIPs results from [5] with those of the current study, it is important to note that [5] focused on dry air (13% relative humidity), cylindrical wires, and AC excitations only. In [5], it was shown that for dry air, the $K$ value increases as air pressure decreases to 100 mbar, indicating a larger avalanche size at lower pressures. However, the present study demonstrates that for more humid air—more representative of conditions at cruising altitude—the $K$ value remains relatively stable over a broader range of air pressures, from ground level down to 50 mbar. This is particularly true for excitations involving polarity reversals, such as AC and BP waveforms. This result supports the use of a single fitting parameter, $K$, for predicting PDIV based on SCSIC in aerospace applications.

In comparison with [29], the presented study advances PDIV modeling by extending the SCSIC approach to varying air pressures and three distinct voltage waveforms, including both AC and PWM excitations, whereas [29] restricts its analysis to ground-level conditions under AC excitation alone. Additionally, this work uniquely examines SIPs and their variation across different air pressures, absent in [29]. A critical difference also lies in the treatment of the critical region of $\alpha_{\text{eff}}$ which significantly influences $K$ values according to waveform type—a factor not addressed in [29]. This omission may lead to similar PDIV predictions across AC, BP, and UP excitations, introducing potential inaccuracies. Furthermore, the current study offers novel insights into PD localization in rectangular insulated wires, particularly emphasizing the significance of fillet radius and insulation thickness, aspects overlooked in [29]. The results underscore that the $K$ values derived in [29] are specific to ground-level AC conditions and cannot be directly applied to the conditions analyzed here.

### C. PDIV PREDICTION BASED ON SCSIC

In this section, two $K$ selection methods are compared for predicting the PDIV peak as a function of air pressure to identify the most reliable approach. Fig. 10a shows PDIV predictions using the average $K$ values for each voltage waveform excitation, while Fig. 10b uses unique $K$ values specific to each air pressure and voltage waveform as reported in Fig. 9.

Figs. 10a and 10b show that using a simple average $K$ increases estimation errors. For UP excitations, the maximum error is 35.34% at 10 mbar, and for AC excitations, it is 33.23% at 25 mbar. BP excitations exhibit a maximum negative error of -16.09% at 50 mbar. Despite these discrepancies, PDIV prediction accuracy using average $K$ values remains reasonable at other pressures.

In contrast, Fig. 10b demonstrates PDIV predictions using pressure-adapted $K$ values, which fit very well with the experimental results. The maximum PDIV prediction errors for AC, BP, and UP excitations are −2.16% (at 800 mbar), −2.54% (at 50 mbar), and −3.06% (at 600 mbar), respectively. Using real or pressure-adapted $K$ values yields highly accurate predictions, with consistently negative errors reflecting a conservative approach.

To clarify, the aim of predicting PDIV using two approaches—(1) the average $K$ values across different air pressures for a specific excitation (Fig. 10a), and (2) the pressure-adapted $K$ value for each voltage excitation—is to highlight the differences in prediction accuracy. While using an average $K$ value results in higher prediction errors, applying the pressure-adapted $K$ value for specific air pressures, such as those corresponding to cruising altitudes in aerospace applications, significantly improves accuracy. The remaining errors in Fig. 10b stem from inherent limitations in the mathematical model.

Numerous factors influence PDIV, making it impractical to model each one individually, as this would overcomplicate the prediction model and reduce its reliability.

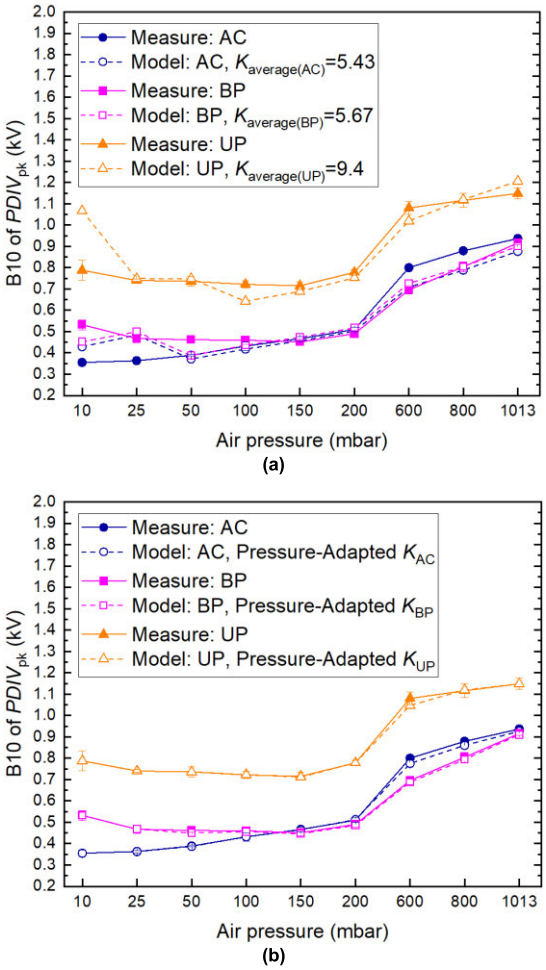


**FIGURE 10. PDIV prediction evaluation using (a) average *K* values obtained from 1013 mbar to 10 mbar, and (b) pressure-adapted *K* under three distinct excitations (AC, BP, and UP) as a function of air pressure.**

Instead, their combined effects are captured in a single fitting parameter, like $K$. For instance, the fast rise time of steep-fronted voltage waveforms, together with electron firing delay, can lead to higher PDIV. However, once PD

occurs, rapid voltage rise limits charge diffusion, allowing deposited charges to trigger stable PD activity, potentially lowering PDIV with faster rise times. Similarly, high switching frequencies reduce charge dissipation time, sustaining PD activity and lowering PDIV, though extremely high frequencies may suppress orientation polarization, reduce permittivity, and increase PDIV by weakening field intensity in air gaps. Environmental factors like air pressure, humidity, and temperature also affect PDIV by influencing air ionization, permittivity, and the surface conductivity of solid insulation, further altering field intensity and PDIV.

Thus, when PDIV values are used to derive $K$ under specific conditions, all these influences are inherently considered. As PDIV is a multiphysics parameter, using $K$ simplifies the complexity of its prediction. Different $K$ values obtained for sinusoidal or square waveforms at various air pressures lead to distinct PDIV predictions using the SCSIC method.

The fundamental differences in modeling PDIV under AC and PWM excitations, primarily attributed to varying $K$ values. It is demonstrated that $K$ values differ not only between AC and PWM but also among BP and UP excitations. Specifically, the relationship $K_{AC} < K_{BP} < K_{UP}$ highlights that using $K_{AC}$ for PWM predictions may lead to conservative estimates, while $K_{UP}$ for AC or BP conditions could yield significant overestimations. The findings underscore the necessity of distinct $K$ values for accurate PDIV modeling across different excitation types. This difference arises from the correlation between PDIV values and the dispersion of the critical region of $\alpha_{eff}$. As shown in Fig. 6, the critical region of $\alpha_{eff}$ becomes less dense and broader, shifting towards electric field lines with lower intensity as the air pressure reduces. Consequently, the PDIV variations between AC and PWM excitations result in distinct $K$ values as air pressure changes. Although the model structure may appear similar for both excitations, the key factor is the relationship between the dispersion of $\alpha_{eff}$ due to air pressure variations and the different PDIV values under each excitation.

This study examines the feasibility of PDIV modeling using a single fitting parameter, $K$, derived from the average values obtained under AC, BP, and UP excitations (Fig. 10a). The results demonstrate significant PDIV estimation errors at air pressures below 50 mbar, particularly for UP excitations at 10 mbar. $K$ is shown to be dependent on the voltage waveform, with unipolar excitations yielding higher $K$ values than AC and BP excitations. As illustrated in Fig. 9, the variation in $K$ with air pressure is subtle for waveforms with polarity reversal (AC and BP) down to 50 mbar. However, at lower air pressures, the differences in $K$ values between AC and BP excitations become more pronounced. Thus, $K$ exhibits noticeable variations at pressures below 50 mbar, depending on the voltage waveform.

In [28], it was demonstrated that the variation in $K$ across different magnet wires is negligible at ground level. Although $K$ values differ among various magnet wires, these differences are minor, permitting an average $K$ value of 5.98 for PDIV prediction. This finding suggests that negligible variations in $K$ imply that the SCSIC could be an effective approach for predicting PDIV.

In contrast, this study shows that $K$ remains relatively stable from ground level to 50 mbar, particularly for excitation types with polarity reversals (e.g., AC and bipolar), despite variations in PDIV with changing air pressure. This quasi-stability of $K$ confirms the robustness of the SCSIC for predicting PDIV across different pressures.

Notably, [28] focused on cylindrical insulated wires at ground level, while this study examines rectangular insulated wires at varying air pressures. Additionally, [28] did not analyze SIPs and primarily concentrated on AC excitations, whereas this study investigates two types of PWM excitations—UP and BP—in comparison with AC excitations.

Compared to the analytical approach in [8], which predicts PDIV as a function of air pressure, the PDIV model developed in this study, based on SCSIC, demonstrates higher accuracy. While the model in [8] is limited to AC excitations, the model presented here accounts for both AC and PWM excitations, including BP and UP waveforms. Importantly, [8] does not provide a quantified estimation error for PDIV, making a direct quantitative comparison between the two models impractical. Another key difference between the two studies is the behavior of AC PDIV under decreasing air pressure. In this study, AC PDIV consistently decreases as pressure is reduced to 10 mbar. However, [8] reports an increase in PDIV when the pressure is lowered from 20–30 mbar to 10 mbar. A possible explanation for this discrepancy is the extended 30-minute waiting time between voltage increments applied in this study at 10 mbar, which likely increases the likelihood of PD inception at low pressures. This extended waiting time was introduced to improve accuracy, though it remains a hypothesis, as the waiting time at 10 mbar was not reported in [8], preventing direct comparison.

The combined effects of temperature and humidity on $K$ and PDIV modeling at ground level using SCSIC were thoroughly investigated in [21] and [35]. Key findings from this study indicate that $K$ varies with humidity, exhibiting distinct patterns at low and high temperatures. Additionally, it was observed that at elevated temperatures, a transition phase occurs as a function of relative humidity, resulting in significant changes in SIP due to the disappearance of a critical region in $\alpha_{eff}$ at specific electric field intensities.

### D. CFLL

Fig. 11 shows the CFLL values under PDIV as a function of air pressure for different voltage waveform excitations. CFLL is the length of the electric field line where maximum $K$ values are obtained under PDIV. Fig. 11 demonstrates that CFLL increases consistently with decreasing air pressure. A longer CFLL results in higher kinetic energy for the electrons at the head of an avalanche, leading to more harmful PD activity. This damage can reach levels that even corona-resistant

insulating materials cannot withstand for more than one hour at reduced air pressures [5].

The ratios of CFLL at 10 mbar to 1013 mbar for AC, BP, and UP excitations are 157.6, 173.17, and 125.72, respectively. This indicates that as air pressure decreases, the harmfulness associated with PD activity increases more rapidly for voltage excitations with polarity reversal (i.e., AC and BP). Fig. 11 shows that at each air pressure, the CFLL values for AC and BP excitations are almost comparable, while the CFLL for UP excitations is longer.

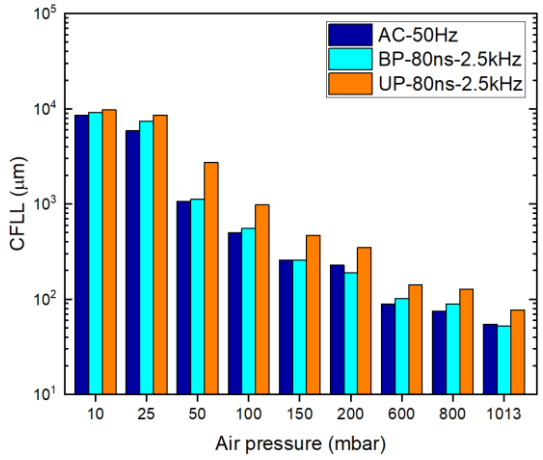


**FIGURE 11.** CFLL variations as a function of air pressure for three distinct excitations (AC, BP, and UP).

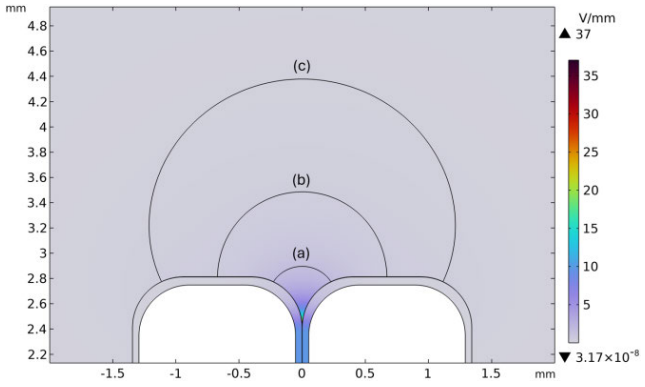


**FIGURE 12.** Typical CFLL (discharge) locations: (a) Close fillet for AC and BP excitations from 1013 mbar to 50 mbar, and UP excitations from 1013 mbar to 100 mbar; (b) Edgewise side for UP excitations at 50 mbar; (c) Far fillet for all voltage waveform excitations at 25 mbar and 10 mbar.

However, the CFLL promotion rate for UP excitations from 1013 mbar to 10 mbar is lower than for AC and BP excitations, with a ratio of 125.72 at 10 mbar to 1013 mbar. Thus, at the lowest air pressure (10 mbar), the CFLL values for UP and BP excitations become comparable.

For PD localization, Fig. 12 depicts the typical CFLL (discharge site) positions in rectangular wire turn-to-turn insulation under different voltage waveforms and air pressures. CFLL is typically found at the fillet sides—either the close fillet at higher air pressures (Fig. 12, filed line (a)) or the far fillet at lower air pressures (Fig. 12, filed line (c)). For AC and BP excitations, from 1013 mbar to 50 mbar, CFLL is found at the close fillet (Fig. 12, filed line (a)). The same applies to UP excitations, except at 50 mbar, where CFLL is found on the edgewise side between the close and far fillets (Fig. 12, filed line (b)). For all voltage waveform excitations, CFLL is found at the far fillet at 25 and 10 mbar, reflecting a longer CFLL (Fig. 12, filed line (c)). When the maximum $K$ values (i.e., avalanche size) and CFLL often occur at the fillet sides, this highlights the important role of the fillet side in PD characteristics and PD phenomenology for rectangular insulated wires. Consequently, wire manufacturers should consider optimizing the fillet radius and insulation thickness at the fillet sides in the design and manufacturing of rectangular insulated wires [11], [36].

### E. EFFECTIVE IONIZATION COEFFICIENT

Fig. 13 indicates the effective ionization coefficient ($\alpha_{\text{eff}}$) corresponding to the CFLL, where $K$ reaches its highest value under PDIV. Fig. 13 reports $\alpha_{\text{eff}}$ values as a function of air pressure for different voltage waveform excitations. As shown, $\alpha_{\text{eff}}$ decreases as air pressure reduces, displaying an opposite trend compared to CFLL variations concerning air pressure. The ratios of $\alpha_{\text{eff}}$ at ground level (1013 mbar) to 10 mbar under AC, BP, and UP excitations are 203.08, 156.34, and 131.19, respectively. This indicates that the rate of $\alpha_{\text{eff}}$ reduction from 1013 mbar to 10 mbar depends on the voltage waveform excitation, with the most significant reduction under AC excitation and the least under UP excitation.

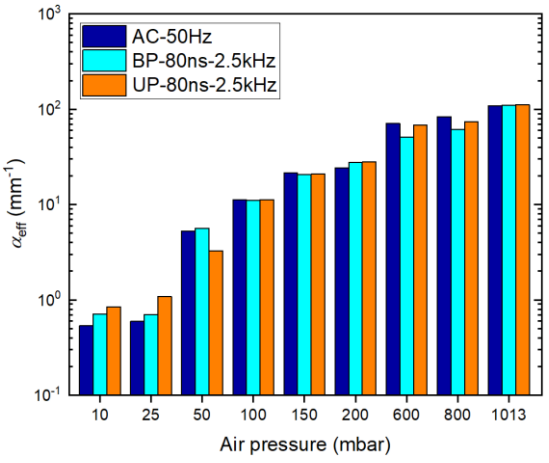


**FIGURE 13.** The variations of effective ionization coefficient as a function of air pressure for three distinct excitations (AC, BP, and UP).

Fig. 13 shows that the obtained $\alpha_{\text{eff}}$ value at each specific air pressure is almost independent of the waveform excitation, giving comparable values for AC, BP, and UP excitations. However, from 50 mbar down to 10 mbar, $\alpha_{\text{eff}}$ values change with the voltage waveform excitation. For example, at the lowest air pressure (10 mbar), $\alpha_{\text{eff}}$is higher for PWM excitations than for AC. It should be noted that a higher $\alpha_{\text{eff}}$ for PWM excitations does not result in a lower PDIV compared

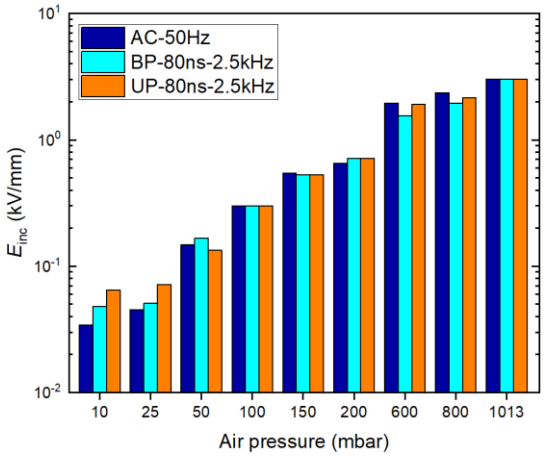


**FIGURE 14.** The variations of PD inception field as a function of air pressure for three distinct excitations (AC, BP, and UP).

to AC; conversely, PDIV at 10 mbar is higher for PWM excitations. This can be attributed to the fast rise time of PWM excitation and the reduced probability of the first electron availability to initiate PD at lower air pressures, where the gas number density is lower, limiting the avalanche size from reaching its critical value to incept PD.

### F. PD INCEPTION FIELD

Fig. 14 illustrates the electric field intensity across CFLL ($E_{inc}$), where maximum $K$ values are achieved under PDIV, as a function of air pressure for various voltage waveform excitations. $E_{inc}$ weakens with decreasing air pressure, showing a direct correlation with $\alpha_{eff}$ (Fig. 13) and an inverse correlation with CFLL (Fig. 11). The ratio of $E_{inc}$ at 1013 mbar to 10 mbar is 88.07, 63.2, and 46.96, under AC, BP, and UP

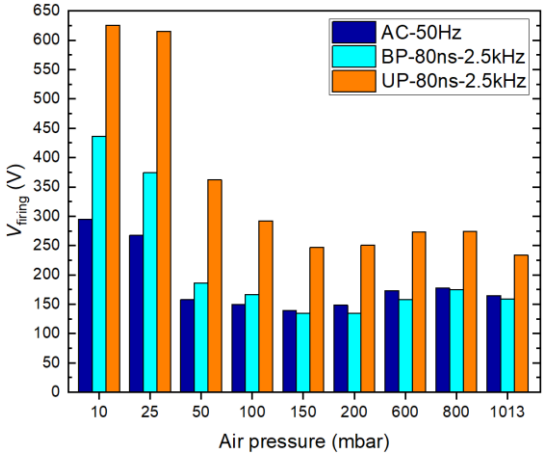


**FIGURE 15.** The variations of firing voltage as a function of air pressure for three distinct excitations (AC, BP, and UP).

excitations, respectively. This suggests that the rate of $E_{inc}$ reduction from 1013 mbar to 10 mbar is highest and lowest under AC and UP excitations, respectively. For instance, under AC, $E_{inc}$ decreases from 3.02 kV/mm at 1013 mbar to 0.03 kV/mm at 10 mbar, while under UP excitations, $E_{inc}$ decreases from 3.02 kV/mm at 1013 mbar to 0.06 kV/mm at 10 mbar. From 1013 mbar to 200 mbar (cruising altitude of 38.6k ft), $E_{inc}$ decreases by 4.65, 4.22, and 4.23 under AC, BP, and UP excitations, respectively, indicating a larger reduction rate in AC and a comparable reduction rate under PWM excitations. Similar to $\alpha_{eff}$, from 1013 mbar down to 100 mbar, $E_{inc}$ is nearly independent of voltage waveform excitation. However, at lower air pressures, from 50 to 10 mbar, $E_{inc}$ varies for different voltage waveform excitations.

### G. FIRING VOLTAGE

Fig. 15 depicts the variation of the firing voltage ($V_{firing}$), the voltage corresponding to CFLL, as a function of air pressure for different voltage waveform excitations. $V_{firing}$ is calculated by multiplying CFLL (Fig. 11) by $E_{inc}$ (Fig. 14). A linear relationship exists between $V_{firing}$ and PD charge amplitude, where higher $V_{firing}$ implies a larger PD charge magnitude [12], [37].

Fig. 15 shows that $V_{firing}$ remains relatively stable from 1013 mbar down to 150 mbar, with average values of 160.54 V, 152.17 V, and 255.65 V under AC, BP, and UP excitations, respectively. However, below 100 mbar, $V_{firing}$ increases with air pressure reduction. For air pressures lower than 100 mbar, both $V_{firing}$ and CFLL (Fig. 11) increase considerably, resulting in a significant rise in harmfulness associated with PD activity. Longer CFLL implies higher kinetic energy of electrons at the avalanche head, while higher $V_{firing}$ implies a larger avalanche size, highlighting significant damage associated with PD activity below 100 mbar.

To quantify the promotion of $V_{firing}$ from 150 mbar downwards to 10 mbar, the ratio of $V_{firing}$ at 10 mbar to 150 mbar can be calculated. This ratio is 2.12, 3.24, and 2.53 for AC, BP, and UP excitations, respectively. Thus, from 150 mbar down to 10 mbar, the highest promotion of $V_{firing}$ or PD charge amplitude is attributed to PWM, particularly BP excitations.

Fig. 15 also shows that at each air pressure, $V_{firing}$ values under UP excitations are higher than those under BP and AC excitations, indicating a higher PD charge amplitude under UP excitations. Comparing $V_{firing}$ in AC with $V_{firing}$ under BP excitation, they are comparable from 1013 mbar downwards to 150 mbar, with $V_{firing}$ in AC slightly higher. However, below 100 mbar, $V_{firing}$ under BP becomes higher than $V_{firing}$ under AC excitations. The difference between $V_{firing}$ under BP and AC excitations becomes significant at the lowest air pressure (10 mbar). The ratio of $V_{firing}$ under BP to AC is 1.11 at 100 mbar, increasing to 1.48 at 10 mbar.

## V. CONCLUSION

This study presents a novel investigation into the partial discharge (PD) behavior in rectangular turn-to-turn insulation of inverter-fed motors under varying air pressures, utilizing both AC 50 Hz and PWM (BP and UP) excitations. A key

contribution of this work is the development of a predictive PDIV model based on Schumann's streamer inception criterion (SCSIC), which uniquely accounts for air pressure variations across different voltage waveforms.

The first major novelty of this study is its demonstration of how PDIV peak and peak-to-peak values under PWM excitations differ from AC PDIV values as a function of air pressure. The experimental findings provide crucial insights: for insulation testing in inverter-fed motors, using PDIV peak-to-peak as the test voltage shows that AC excitations offer more conservative reference criteria across air pressures from 1013 mbar to 10 mbar, consistently resulting in lower PDIV values than PWM excitations. At air pressures below 800 mbar, PDIV peak-to-peak values for BP and UP excitations, with the same switching frequency and rise time, are comparable. Under AC conditions, both PDIV peak and peak-to-peak values decrease steadily with pressure, whereas for PWM excitations, the values decrease only down to 150 mbar before rising again at lower pressures.

For PD-free design, where PDIV peak is used instead of peak-to-peak values, the study reveals that at 200 mbar, 150 mbar, and 1013 mbar, PDIV peak values under AC and BP excitations are comparable, though slightly lower for BP. However, relying solely on AC excitation PDIV peak values for aerospace and automotive applications is shown to be risky, especially at 800 and 600 mbar, where AC PDIV peak values are significantly less reliable. Hence, for air pressures between ground level and 200 mbar, PDIV peak values under the same PWM excitation as used in practice are recommended. The study also reveals that PDIV peak values under UP excitations are higher than those under BP and AC across all air pressures, indicating that using AC excitation values for design could result in overly conservative designs, particularly in automotive and aerospace contexts.

Another important contribution of this work is the introduction of the pressure-adapted $K$ values in the PDIV predictive model, which closely match experimental results. The model achieves low PDIV prediction errors: -2.16% at 800 mbar, -2.54% at 50 mbar, and -3.06% at 600 mbar for AC, BP, and UP excitations, respectively, whereas higher errors are observed when using a simple $K$ average.

A further novelty of this research is the detailed analysis of SIPs as a function of air pressure for AC, BP, and UP excitations. The study demonstrates that as air pressure decreases, the CFLL increases more rapidly for voltage excitations with polarity reversal (AC and BP). Furthermore, maximum $K$ values, indicating the highest avalanche size, and CFLL often occur at the fillet sides, highlighting the importance of optimizing the fillet radius and insulation thickness in rectangular insulated wire designs. Additionally, $\alpha_{\text{eff}}$ and $E_{\text{inc}}$ decrease with air pressure, with $\alpha_{\text{eff}}$ showing the most significant reduction under AC excitation and the least under UP. Meanwhile, $V_{\text{firing}}$ remains relatively stable down to 150 mbar but increases below 100 mbar, significantly raising PD charge amplitude and discharge energy, indicating a heightened risk of PD damage at very low pressures.

These findings offer important insights for the design and testing of insulation systems in inverter-fed motors, especially in aerospace environments where air pressure is reduced. The novel PDIV model and SIP analysis provide practical guidance for developing robust PD-free insulation designs that can withstand varying pressure conditions.

## REFERENCES


[1] *Rotating Electrical Machines—Part 18-41: Partial Discharge Free Electrical Insulation Systems (Type I) Used in Rotating Electrical Machines Fed From Voltage Converters—Qualification and Quality Control Tests*, IEC Standard 60034-18-41, 2019.

[2] A. Cavallini, D. Fabiani, and G. C. Montanari, "Power electronics and electrical insulation systems—Part 1: Phenomenology overview," *IEEE Elect. Insul. Mag.*, vol. 26, no. 3, pp. 7–15, May 2010.

[3] *Rotating Electrical Machines—Part 18-42: Qualification and Acceptance Tests for Partial Discharge Resistant Electrical Insulation Systems (Type II) Used in Rotating Electrical Machines Fed From Voltage Converters*, IEC Standard 60034-18-42, 2016.

[4] A. Rumi, J. G. Marinelli, D. Barater, A. Cavallini, and P. Seri, "The challenges of reliable dielectrics in modern aerospace applications: The hazard of corona resistant materials," *IEEE Trans. Transport. Electrific.*, vol. 8, no. 4, pp. 4646–4653, Dec. 2022.

[5] H. Naderiallaf, Y. Ji, P. Giangrande, and M. Galea, "Air pressure impact on the avalanche size for turn-to-turn insulation of inverter-fed motors," *IEEE Trans. Dielectr. Elect. Insul.*, vol. 31, no. 1, pp. 85–94, Feb. 2024.

[6] P. Mancinelli, S. Stagnitta, and A. Cavallini, "Qualification of hairpin motors insulation for automotive applications," *IEEE Trans. Ind. Appl.*, vol. 53, no. 3, pp. 3110–3118, May 2017.

[7] X. Ju, Y. Cheng, M. Yang, S. Cui, A. Sun, X. Liu, and M. He, "Voltage stress calculation and measurement for hairpin winding of EV traction machines driven by SiC MOSFET," *IEEE Trans. Ind. Electron.*, vol. 69, no. 9, pp. 8803–8814, Sep. 2022.

[8] L. Lusuardi, A. Rumi, A. Cavallini, D. Barater, and S. Nuzzo, "Partial discharge phenomena in electrical machines for the more electrical aircraft. Part II: Impact of reduced pressures and wide bandgap devices," *IEEE Access*, vol. 9, pp. 27485–27495, 2021.

[9] A. Rumi, A. Cavallini, and L. Lusuardi, "Impact of WBG converter voltage rise-time and switching frequency on the PDIV of twisted pairs," in *Proc. IEEE 3rd Int. Conf. Dielectr. (ICD)*, Valencia, Spain, Jul. 2020, pp. 902–905.

[10] C. He, M. Beltle, S. Tenbohlen, T. Hubert, S. Schmidt, and J. Schneider, "Partial discharge characteristic of hairpin windings for inverter-fed motors," in *Proc. IEEE 4th Int. Conf. Dielectr. (ICD)*, Palermo, Italy, Jul. 2022, pp. 49–52.

[11] H. Naderiallaf, M. Degano, C. Gerada, and D. Gerada, "Fillet radius impact of rectangular insulated wires on PDIV for turn-to-turn insulation of inverter-fed motors," *IEEE Trans. Dielectr. Elect. Insul.*, vol. 31, no. 4, pp. 2084–2093, Aug. 2024.

[12] H. Naderiallaf, M. Degano, and C. Gerada, "PDIV modelling for rectangular wire turn-to-turn insulation of inverter-fed motors through thermal ageing," *IEEE Trans. Dielectr. Elect. Insul.*, vol. 31, no. 1, pp. 550–559, Feb. 2024.

[13] H. Naderiallaf, M. Degano, and C. Gerada, "Assessment of edgewise insulated wire bend radius impact on dielectric properties of turn-to-turn insulation through thermal ageing," *IEEE Trans. Dielectr. Elect. Insul.*, vol. 31, no. 1, pp. 419–428, Feb. 2024.

[14] Z. Guo, A. Q. Huang, R. E. Hebner, G. C. Montanari, and X. Feng, "Characterization of partial discharges in high-frequency transformer under PWM pulses," *IEEE Trans. Power Electron.*, vol. 37, no. 9, pp. 11199–11208, Sep. 2022.

[15] V. Madonna, P. Giangrande, W. Zhao, H. Zhang, C. Gerada, and M. Galea, "Electrical machines for the more electric aircraft: Partial discharges investigation," *IEEE Trans. Ind. Appl.*, vol. 57, no. 2, pp. 1389–1398, Mar. 2021.

[16] D. Evans, J. Knaster, and H. Rajainmaki, "Vacuum pressure impregnation process in superconducting coils: Best practice," *IEEE Trans. Appl. Supercond.*, vol. 22, no. 3, Jun. 2012, Art. no. 4202805.

[17] H. Naderiallaf, Y. Ji, P. Giangrande, and M. Galea, "Temperature impact on PDIV for turn-to-turn insulation of inverter-fed motors: From ground level to cruising altitude," *IEEE Trans. Dielectr. Elect. Insul.*, vol. 31, no. 2, pp. 1044–1053, Apr. 2024.

[18] H. Naderiallaf, R. Ghosh, P. Seri, and G. C. Montanari, "HVDC insulation systems: Effect of voltage polarity inversion slew rate on partial discharge phenomenology and harmfulness," in *Proc. 22nd Int. Symp. High Voltage Eng. (ISH )*, Xi'an, China, Nov. 2021, pp. 7–12.
[19] M. Goldman, A. Goldman, and J. Gatellet, "Physical and chemical aspects of partial discharges and their effects on materials," in *Proc. Int. Conf. Partial Discharge*, 1993, pp. 11–14.
[20] H. Naderiallaf, P. Giangrande, and M. Galea, "A contribution to thermal ageing assessment of glass fibre insulated wire based on partial discharges activity," *IEEE Access*, vol. 10, pp. 41186–41200, 2022.
[21] H. Naderiallaf, Y. Ji, P. Giangrande, and M. Galea, "Modeling humidity impact on PDIV for turn-to-turn insulation of inverter-fed motors at different temperatures," *IEEE Trans. Dielectr. Elect. Insul.*, vol. 31, no. 3, pp. 1573–1582, Jun. 2024.
[22] H. Naderiallaf, P. Giangrande, and M. Galea, "Experimental considerations on the possible impact of space charge accumulation on partial discharges activity for wire insulations," in *Proc. IEEE 4th Int. Conf. Dielectr. (ICD)*, Palermo, Italy, Jul. 2022, pp. 82–85.
[23] H. Raether, *Electron Avalanches and Breakdown in Gases*. London, U.K.: Butterworth, 1964.
[24] W. O. Schumann, "Über das minimum der durchbruchfeldstärke bei kugelelektroden," *Arch. Elektrotech.*, vol. 12, nos. 6–12, pp. 593–608, Jun. 1923.
[25] G. J. M. Hagelaar and L. C. Pitchford, "Solving the Boltzmann equation to obtain electron transport coefficients and rate coefficients for fluid models," *Plasma Sources Sci. Technol.*, vol. 14, no. 4, pp. 722–733, Nov. 2005.
[26] *BOLSIG+ | Electron Boltzmann Equation Solver*. Accessed: Mar. 20, 2023. [Online]. Available: http://www.bolsig.laplace.univ-tlse.fr/
[27] H. Naderiallaf, P. Giangrande, and M. Galea, "Characterization of PDIV, PDEV, and RPDIV in insulated wires under unipolar repetitive square wave excitations for inverter-fed motors," *IEEE Access*, vol. 11, pp. 51047–51063, 2023.
[28] L. Lusuardi, A. Cavallini, M. G. de la Calle, J. M. Martínez-Tarifa, and G. Robles, "Insulation design of low voltage electrical motors fed by PWM inverters," *IEEE Elect. Insul. Mag.*, vol. 35, no. 3, pp. 7–15, May 2019.
[29] J. Gao, A. Rumi, Y. He, and A. Cavallini, "Towards a holistic approach to inverter-fed machine design: FEM-based PDIV prediction of complete windings," *IEEE Trans. Dielectr. Electr. Insul.*, vol. 30, no. 6, pp. 2870–2877, Dec. 2023.
[30] L. Lusuardi, "Towards a partial discharge free insulation system for the more electrical transportation," Ph.D. dissertation, Dipartimento di Ingegneria dell'Energia Elettrica e dell'Informazione 'Guglielmo Marconi', Univ. Bologna, Bologna, Italy, Mar. 2020.
[31] D. Fabiani, G. C. Montanari, A. Cavallini, and G. Mazzanti, "Relation between space charge accumulation and partial discharge activity in enameled wires under PWM-like voltage waveforms," *IEEE Trans. Dielectr. Elect. Insul.*, vol. 11, no. 3, pp. 393–405, Jun. 2004.
[32] P. Wang, H. Xu, J. Wang, W. Zhou, and A. Cavallini, "The influence of repetitive square wave voltage rise time on partial discharge inception voltage," in *Proc. IEEE Conf. Electr. Insul. Dielectric Phenomena (CEIDP)*, Toronto, ON, Canada, Oct. 2016, pp. 759–762.
[33] A. Rumi, L. Lusuardi, A. Cavallini, M. Pastura, D. Barater, and S. Nuzzo, "Partial discharges in electrical machines for the more electrical aircraft. Part III: Preventing partial discharges," *IEEE Access*, vol. 9, pp. 30113–30123, 2021.
[34] A. Cavallini, D. Fabiani, and G. C. Montanari, "Power electronics and electrical insulation systems—Part 3: Diagnostic properties," *IEEE Elect. Insul. Mag.*, vol. 26, no. 5, pp. 30–40, Sep. 2010.
[35] H. Naderiallaf, Y. Ji, P. Giangrande, M. Galea, M. Degano, and C. Gerada, "Humidity impact on streamer inception parameters for turn-to-turn insulation of inverter-fed motors," in *Proc. IEEE 5th Int. Conf. Dielectr. (ICD)*, Toulouse, France, Jun./Jul. 2024, pp. 1–4.
[36] H. Naderiallaf, C. Gerada, M. Degano, and D. Gerada, "PDIV modeling for rectangular wire turn-to-turn insulation of inverter-fed motors at different cruising altitudes," in *Proc. Int. Conf. Elect. Mach. (ICEM)*, Torino, Italy, Sep. 2024, pp. 1–7.
[37] P. Seri, H. Naderiallaf, and G. C. Montanari, "Modelling of supply voltage frequency effect on partial discharge repetition rate and charge amplitude from AC to DC at room temperature," *IEEE Trans. Dielectr. Electr. Insul.*, vol. 27, no. 3, pp. 764–772, Jun. 2020.

**HADI NADERIALLAF** was born in Mashhad, Iran, in April 1986. He received the M.Sc. degree in electrical engineering with a specialization in high voltage engineering from Leibniz University Hannover, Germany, in 2012, and the Ph.D. degree in electrical engineering with a specialization in high voltage engineering from the University of Bologna, Italy, in 2021. In 2019, he was a Visiting Scholar and the Ph.D. Researcher with the Department of High Voltage Engineering, Technical University of Berlin, Germany, for three months. With five years of working experience in the field, he specializes in HV transformer oil reclamation. Since April 2021, he has been a Postdoctoral Research Fellow with the University of Nottingham, U.K. He is currently engaged in research on electrical machine insulation design and reliability aspects for industrial projects, including aerospace and automotive applications. His research interests include electrical insulating materials, ac, dc, and PWM partial discharge detection and modeling, insulation systems' reliability for electrical machines, HVDC cable design, multiphysics modeling, space charge measurement and analysis, condition monitoring techniques, DGA, and transformer oil reclamation.

**MICHELE DEGANO** (Senior Member, IEEE) received the master's degree in electrical engineering from the University of Trieste, Italy, in 2011, and the Ph.D. degree in industrial engineering from the University of Padova, Italy, in 2015. From 2014 to 2016, he was a Postdoctoral Researcher with the University of Nottingham, U.K., where he joined the Power Electronics, Machines and Control (PEMC) Research Group. In 2016, he was an Assistant Professor of advanced electrical machines with the University of Nottingham, U.K. He was promoted to an Associate Professor, in 2020, and a Professor, in 2022, leading research projects for the development of future hybrid electric aerospace platforms and electric transport. He is currently the Chief Engineer of Nottingham Drives Specialist Services (NDSS), University of Nottingham, a business unit dedicated to supporting the industrialization of electrical machines and drives. He is the author/co-author of more than 150 scientific articles. His research interests include electrical machines and drives for industrial, automotive, railway, and aerospace applications, ranging from small to large power.

**CHRISTOPHER GERADA** (Senior Member, IEEE) received the Ph.D. degree in numerical modeling of electrical machines from the University of Nottingham, Nottingham, U.K., in 2005. He is currently the Head of the University of Nottingham Zero Carbon Cluster and a Royal Academy of Engineering Research Chair. He established and currently directs the Cummins Innovation Centre. He has led numerous major research consortiums and centers, such as GE Aviation UTSP, FIRST-Advance Propulsion Centre, and Actuation2115. Throughout his career, he has secured over £50 million in funding through major industrial, European, and U.K. grants. He has a publication record with over 600 peer-reviewed articles. Before his current roles, he held positions as a Researcher, a Lecturer, an Associate Professor, and a Professor at the University of Nottingham, focusing on high-performance electrical drives and the design and modeling of electromagnetic actuators for aerospace applications. His research interests include the design and modeling of high-performance electric drives and machines. He was a recipient of the Nagamori Awards and has served as the Former Chair of the IEEE IES Electrical Machines Committee. He serves as an Associate Editor for IEEE TRANSACTIONS ON INDUSTRY APPLICATIONS.